Supporting Information

Advanced Energy Storage Device: A Hybrid BatCap System Consisting of Battery-Supercapacitor Hybrid Electrodes Based on a $Li_4Ti_5O_{12}$/Activated-carbon Hybrid Nanotubes

*Hong Soo Choi, Ji Hyuk Im, TaeHoon Kim, Jae Hyun Park, Chong Rae Park**

Carbon Nanomaterials Design Laboratory, Global Research Laboratory (GRL), Research Institute of Advanced Materials (RIAM), and Department of Materials Science and Engineering, Seoul National University, Seoul 151-744, Republic of Korea

Corresponding author. Tel: (+82) 2-880-8030. Fax: (+82) 2-885-1748. Email: crpark@snu.ac.kr

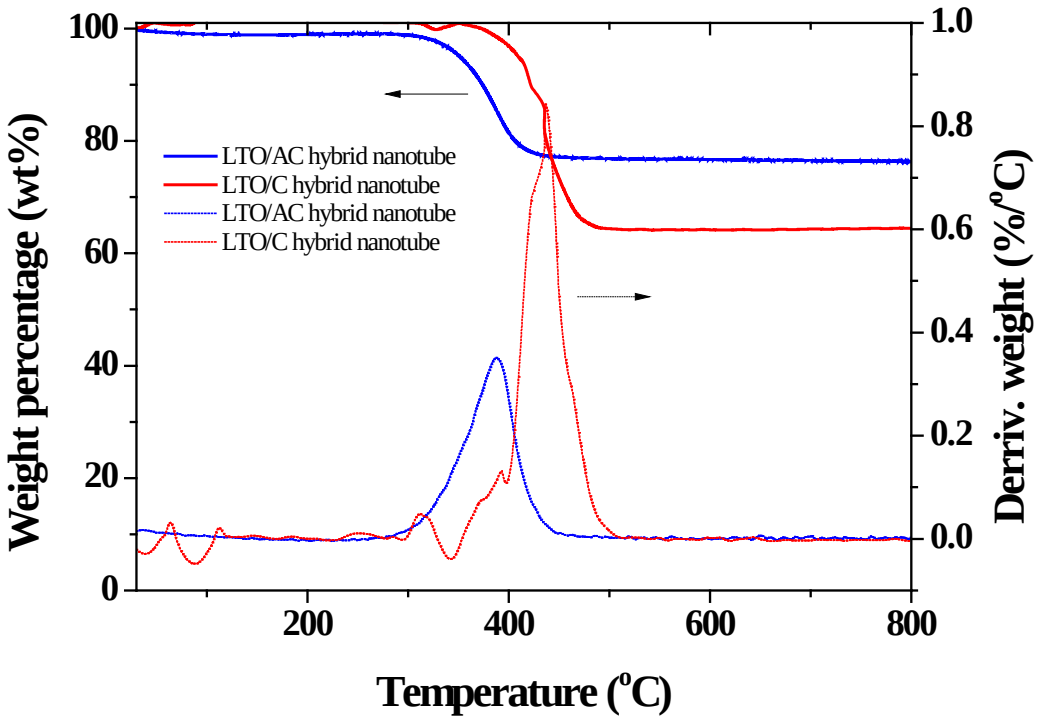

Figure S1. The thermogravimetric analysis (TGA) of the LTO/C-HNS. The solid line indicates the thermogravimetric curve and the dotted line indicates the differential thermogravimetric curve.

Table S1. Residual weight ratios of the LTO/C-HNS series after TGA measurements.

Sample	LTO/AC hybrid nanotubes	LTO/C hybrid nanotubes
Residual weight ratio [wt%]	**78.86**	**64.28**

TGA was carried out to calculate the weight ratio of the lithium titanium oxide phase in the LTO/AC hybrid nanotubes and the LTO/C hybrid nanotubes. These values contributed to the evaluation of the specific surface area of a carbonaceous phase in a composite according to the BET analysis, as shown in Figure 3. The samples were heated from 25°C to 800°C at a heating rate of 5°C min^{-1} under an air flow rate of 100 mL min^{-1}. The residual weight after calcination of each sample is listed in Table S1.

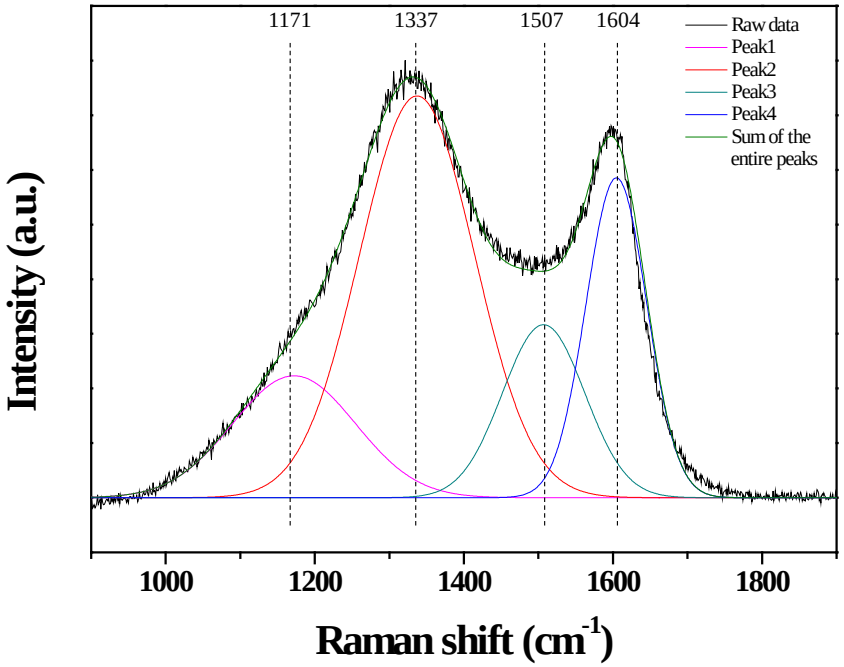

Figure S2. Raman spectrum and curve fitting result for the LTO/AC hybrid nanotubes. Four peaks with peak maxima at 1171, 1337, 1507, and 1604 cm^{-1} were required for the curve description of the Raman spectrum.

Table S2. Deconvolution of the Raman spectrum of the LTO/AC hybrid nanotubes, as shown in Figure S2.

Peak	**Position [cm^{-1}]**	**Area [Area %]**	**Intensity**	**FWHM [cm^{-1})**	**$R=I_{peak2}/I_{peak4}$**
Peak1	1171.8	115543.1 (15.8)	557.8	165.5	1.25
Peak2	1337.4	354979.2 (48.7)	1838.0	154.2	
Peak3	1507.1	109485.1 (15.0)	791.1	110.5	
Peak4	1604.8	149527.2 (20.5)	1463.2	81.6	

The Raman spectrum of the LTO/AC hybrid nanotubes is illustrated in Figure S2 and the curve deconvolution result is listed in Table S2. Peak 1 at position 1171 cm^{-1} arose from the sp^3-rich phase of the amorphous carbon,[1, 2] peak 2 at position 1337 cm^{-1} (D band) arose from highly disordered graphitic structure,[3, 4] peak 3 at position 1337 cm^{-1} arose from the semicircle ring stretch vibration of benzene,[5] and peak 4 at position 1337 cm^{-1} (G band) arose from the sp^2 stretch vibration contribution from the benzene moiety.[3, 4] The curve envelops and peak parameters corresponding to each peak are listed in Table S2.

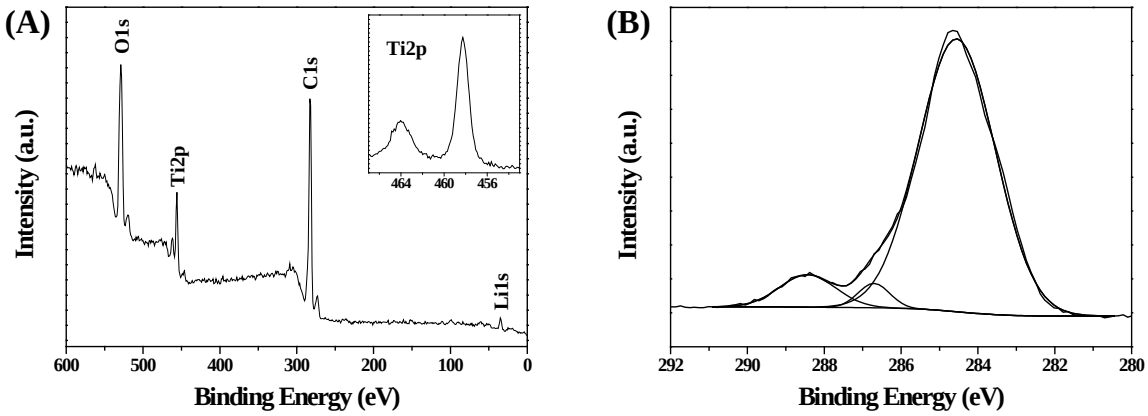

Figure S3. XPS survey spectrum with the inset showing the Ti2p region (A) and the C1s region (B) of the LTO/AC hybrid nanotubes.

Table S3. C1s peak deconvolution of the XPS spectrum in the LTO/AC hybrid nanotubes, as shown in Figure S3B.

Sample	Element	Peak position [eV]	Relative amount of element [Area %]
LTO/AC hybrid nanotubes	C-C and/or C=C	284.55	89.0
	C-O	286.70	3.3
	COO	288.43	7.7

The XPS analysis results of LTO/AC hybrid nanotubes are illustrated in Figure S3. The inset of Figure S3A shows that the Ti2p level consisted of a single doublet due to spin-orbit splitting composed of two symmetric peaks at 464.02 eV and 458.26 eV for the $P_{1/2}$ and $P_{3/2}$ lines, respectively. These results supported the presence of only Ti^{4+} in the $Li_4Ti_5O_{12}$ phase of the composite[6-8] indicating that the $Li_4Ti_5O_{12}$ phase was well synthesized after the preparation procedure for the LTO/AC hybrid nanotubes. Figure S3B shows the C1s spectra of the LTO/AC hybrid nanotubes. The peaks were deconvoluted using a Lorentzian-Gaussian mixed function. The information and the peak parameters are summarized in Table S3. As shown in Figure S3B, the C1s spectrum of the LTO/AC hybrid nanotubes mainly consisted of three peaks at binding energies of 284.55, 286.70, and 288.43 eV, which corresponded to the non-functionalized graphitic carbon (C-sp^2 and/or -sp^3 bondings), the C-O of

ether/hydroxyl groups, and the COO of the carboxyl/lactone groups, respectively.[9-11] These results indicated the absence of a carbon peak corresponding to the carbonyl/quinone groups through the LiCl-assisted air-activation process for PVA. Also, the element data, normalized by the area ratio of each peak in Table S3, shows that graphitic carbon clearly provided the most dominant carbon structure, at about 78% in the LTO/AC hybrid nanotubes, due to the use of the LiCl-assisted air-activation process.

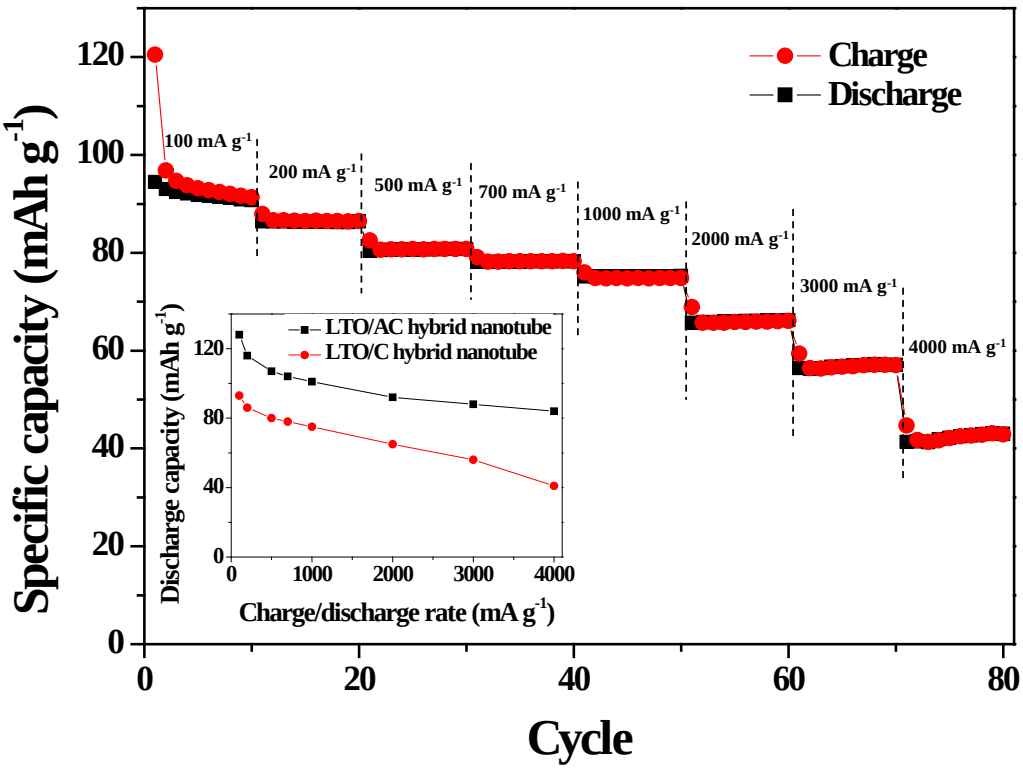

Figure S4. Cycle performances of the LTO/C hybrid nanotubes at various charge/discharge rates in the potential range 1.0-2.5 V vs. Li/Li^+. The inset shows the discharge capacity of the LTO/AC hybrid nanotubes and LTO/C hybrid nanotubes at various charge/discharge rates.

Figure S4 shows the cycle performance of the LTO/C hybrid nanotube at various charge/discharge rates as the anode of LIBs. Also, a comparison of the discharge capacity between LTO/AC hybrid nanotubes and LTO/C hybrid nanotubes is displayed in the inset. This indicates that the discharge capacity of the LTO/AC hybrid nanotubes is better than that of the LTO/C hybrid nanotubes at each charge/discharge rate, which illustrates that

the porosity and high surface area of the LTO/AC hybrid nanotubes help to enhance the electrochemical performance due to the better charge transport kinetics.

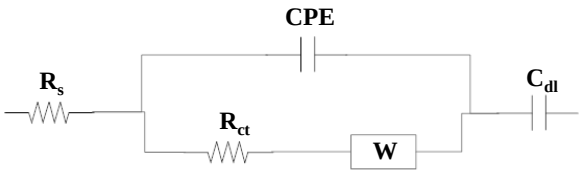

Figure S5. Equivalent circuit evaluated based on the AC impedance spectra of the LTO/AC hybrid nanotubes and pure $Li_4Ti_5O_{12}$.

Table S5. Impedance parameters and Li^+ ion diffusion coefficient calculated from the impedance spectra of the LTO/AC hybrid nanotubes and pure $Li_4Ti_5O_{12}$.

Sample	R_s [Ω g]	R_{ct} [Ω g]	i_0 [mA cm^{-2}]	D_{Li+} [cm^2 s^{-1}]
LTO/AC hybrid nanotubes	5.089 x 10^{-4}	0.058	0.263	9.48 x 10^{-10}
Pure $Li_4Ti_5O_{12}$	3.067 x 10^{-2}	2.632	0.717	2.37 x 10^{-9}

The AC impedance analysis spectra in Figure 5 were fitted using a simple modified Randles–Ershler equivalent circuit[12] as shown in Figure S5 and the related parameters were calculated based on the impedance results listed in Table S5. The electrolyte solution resistance (R_s) was evaluated based on the impedance intercept on the Z-real axis in Figure 5. Furthermore, the charge transfer and Li^+ ion diffusion kinetics were estimated based on the semicircle in the high-middle frequency range and the oblique line of the low frequency range, respectively. The charge transfer resistance at the active material/electrolyte interface (R_{ct}) was evaluated based on the right-hand side intercept impedance intercept on the Z-real axis of the semicircle. Figure S5 indicates the equivalent circuit, where W is the Waburg impedance, CPE is the constant phase element representing the double layer capacitance, and C_{dl} is the insertion capacitance under the applied potential. The Li^+ ion diffusion coefficient, abbreviated

D_{Li+}, was calculated using the following equation[13, 14]:

$$D_{Li^+}^{1/2} = \frac{RT}{2^{1/2} n^2 F^2 A} \times \frac{1}{\sigma C_{Li^+}} \quad (1)$$

where R is the gas constant (R = 8.314 J mol^{-1} K^{-1}), T is the working temperature, n is the number of electrons in the reaction, F is the Faradaic constant (F = 96500 C mol^{-1}), A is the active surface area, and C_{Li+} is the molar concentration of Li in an electrode active material. The Waburg impedance coefficient, denoted σ, may be obtained from the slope of R_{ct} vs. $\omega^{1/2}$ (ω: angular frequency) in the medium frequency range. Also, the values of the exchange current density, abbreviated i_0, in Table S5 were calculated from the following equation.[15]

$$i_0 = \frac{RT}{nFAR_{ct}} \quad (2)$$

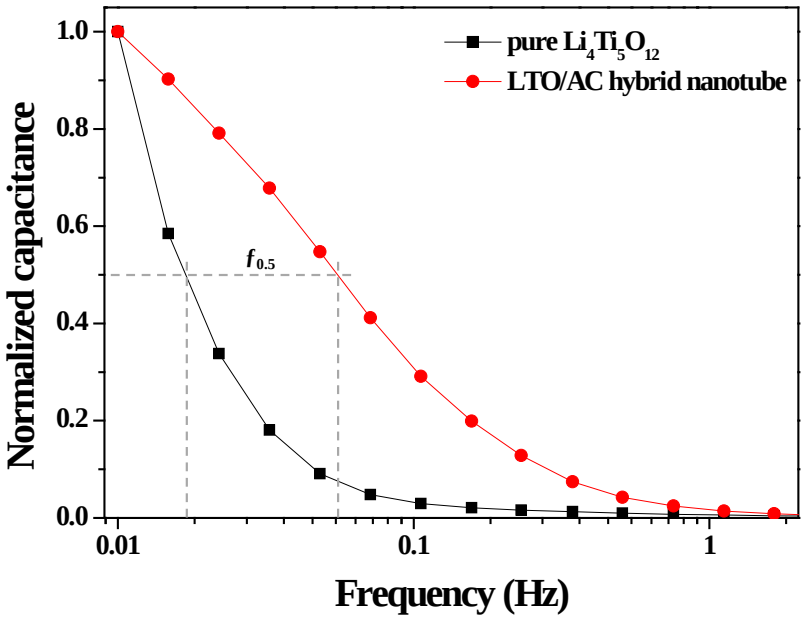

Figure S6. Normalized capacitance and frequency response for the LTO/AC hybrid nanotubes and pure $Li_4Ti_5O_{12}$ half-cells.

The rapid power generation performance of the LTO/AC hybrid nanotubes compared with the pure $Li_4Ti_5O_{12}$ was also demonstrated by comparing the normalized capacitance with the frequency response of each sample in Figure S6. The results indicated that the capacitance dropped to 50% of its maximum value ($f_{0.5}$). The LTO/AC hybrid nanotubes apparently provided a faster frequency response for $f_{0.5}$=0.6 Hz than the pure $Li_4Ti_5O_{12}$ of $f_{0.5}$=0.9 Hz, which results agrees well with the values of D_{Li+} provided in Table S5 with the high rates.[16]

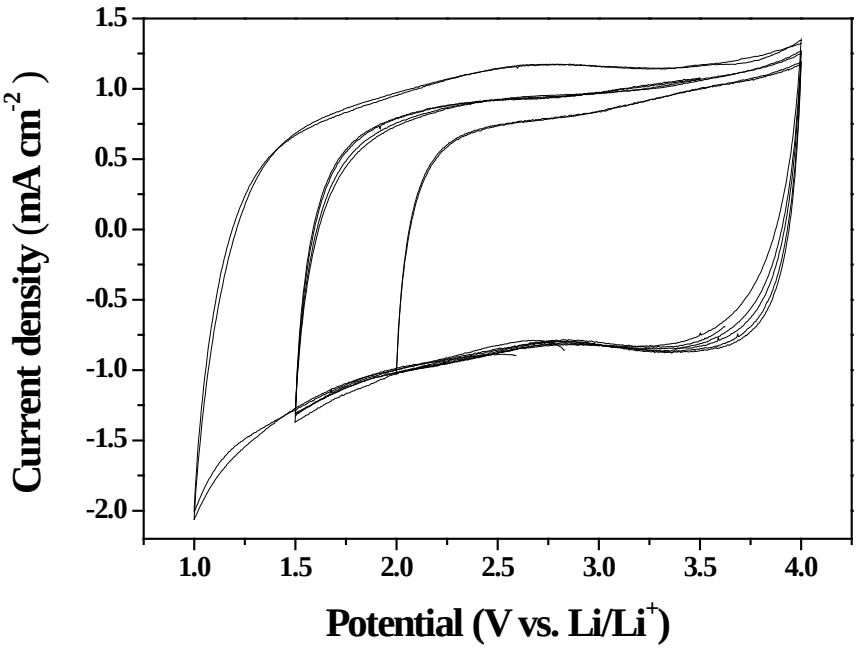

Figure S7. The CV of AC at a 5 mV s^{-1} sweep rate over various potential ranges from 1 to 4 V vs. Li/Li^+ .

The cyclic voltammograms (CVs) of the activated carbon (SX Ultra, denoted as AC) in various potential ranges were measured at a sweep rate of 5 mV s^{-1} with the Li salt-based organic electrolyte (1 M $LiPF_6$ in EC/DEC) to use AC as the positive electrode in the hybrid BatCap system (Figure S7). The resulting curve yielded a typical rectangular shape related to the curve shape for common AC from electrical double layer capacitance (EDLC) by a rotational mirror symmetry operation in the potential range 2.0-4.0 V vs. Li/Li^+. The CV results of the AC indicated that an a solid electrolyte interface (SEI) layer, which closed the open pores on the surface of the AC, thereby limiting the approach of Li^+ ions in the electrolyte, could be formed at applied potentials below 2.0 V vs. Li/Li^+. Besides, the electrolyte decomposition on the surfaces of the AC could be prevented at potentials up to 4.0 V vs. Li/Li^+ of the applied potentials, which caused irreversible specific capacity.[17] Therefore, the CV test

results indicated that AC is and appropriate active material for use in the hybrid BatCap system at a potential range of 2.0-4.0 V vs. Li/Li^+. The calculated capacitance of the AC based on the CV result was 69 F g^{-1}, which provided a specific capacity of 46 mAh g^{-1} at a working potential of 2–4 V vs. Li/Li^+.

1. R. J. Nemanich, J. T. Glass, G. Lucovsky and R. E. Shroder, *J. Vac. Sci. Technol. A-Vac. Surf. Films*, 1988, **6**, 1783-1787.
2. R. E. Shroder, R. J. Nemanich and J. T. Glass, *Phys. Rev. B*, 1990, **41**, 3738-3745.
3. H. S. Choi, T. Kim, J. H. Im and C. R. Park, *Nanotechnology*, 2011, **22**.
4. M. A. Tamor and W. C. Vassell, *Journal of Applied Physics*, 1994, **76**, 3823-3830.
5. N. Colthup, L. Daly and S. Wiberley, *Introduction to Infrared and Raman Spectroscopy*, Academic, New York, 1975.
6. J. Haetge, P. Hartmann, K. Brezesinski, J. Janek and T. Brezesinski, *Chemistry of Materials*, 2011, **23**, 4384-4393.
7. H.-G. Jung, S.-T. Myung, C. S. Yoon, S.-B. Son, K. H. Oh, K. Amine, B. Scrosati and Y.-K. Sun, *Energy & Environmental Science*, 2011, **4**, 1345-1351.
8. Y. Zhao, G. Liu, L. Liu and Z. Jiang, *Journal of Solid State Electrochemistry*, 2009, **13**, 705-711.
9. S.-J. Zhang, H.-Q. Yu and H.-M. Feng, *Carbon*, 2006, **44**, 2059-2068.
10. Z. Yue, C. L. Mangun and J. Economy, *Carbon*, 2004, **42**, 1973-1982.
11. S.-J. Zhang, H.-M. Feng, J.-P. Wang and H.-Q. Yu, *Journal of Colloid and Interface Science*, 2008, **321**, 96-102.
12. K. Dokko, M. Mohamedi, M. Umeda and I. Uchida, *Journal of The Electrochemical Society*, 2003, **150**, A425-A429.
13. M. Shi, Z. Chen and J. Sun, *Cement and Concrete Research*, 1999, **29**, 1111-1115.
14. Y. Li, H. Zhao, Z. Tian, W. Qiu and X. Li, *Rare Metals*, 2008, **27**, 165-169.
15. Y. Shi, L. Wen, F. Li and H.-M. Cheng, *Journal of Power Sources*, 2011, **196**, 8610-8617.
16. L. Wei, M. Sevilla, A. B. Fuertes, R. Mokaya and G. Yushin, *Advanced Energy Materials*, 2011, **1**, 356–361.
17. V. Khomenko, E. Raymundo-Piñero and F. Béguin, *J Power Sources*, 2008, **177**, 643-651.